Effect of Stress on Magnetic Hysteresis Losses in a Switched Reluctance Motor: Application to Stator and Rotor Shrink Fitting

Laurent Bernard and Laurent Daniel

Group of Electrical Engineering–Paris, CNRS(UMR 507)/CentraleSupélec/UPMC/Univ
Paris-Sud Plateau de Moulon, Gif-sur-Yvette F-91192, France

A magnetic hysteresis model is developed based on the vector generalization of Jiles–Atherton (JA) model combined with a simplified multiscale approach to take into account the effect of mechanical stress on the magnetic behavior. The model aims at representing electrical steel behavior under any loading configuration considering the magnetic field vector and the mechanical stress second-order tensor. Mechanical stress is introduced in the JA hysteresis model through the anhysteretic magnetization and a modified pinning parameter. The main properties of the model are shown under alternating and rotating applied induction, especially in terms of hysteresis losses. The differential magnetic susceptibility is derived from the model, and the implementation into a time-stepping finite-element method is detailed. Finally, a quasi-statically rotating switched reluctance motor is studied: considering different shrink-fitting conditions, the resulting stress is shown to have a significant effect on both distribution and global value of hysteresis losses.

Index Terms—**Electrical machines, finite-element method, hysteresis losses, magnetoelasticity, mechanical stress, multiaxiality, multiscale modeling, nonlinearity, time stepping, vector hysteresis.**

I. INTRODUCTION

PERFORMANCE of electrical engineering devices can be estimated at the early design stage from structural analysis models (e.g., using finite elements) and material characterization data (magnetic behavior). A uniform nonlinear anhysteretic magnetic behavior is often considered, and iron losses are evaluated *a posteriori* (postprocessing of structural analysis results). More accurate approaches account for iron losses within the structural analysis. However, iron losses evaluation is generally flawed by the lack of knowledge or accuracy in the representation of the material behavior. In particular, the magnetic behavior is tightly related to the mechanical stress, but this effect is rarely considered. Significant stress levels with sharp local variations arise from iron sheet manufacturing processes, device assembly, or operating conditions, and can have significant effects on the device performance. Few publications address this issue at the structure level.

One of the first attempts was made in [1], where the stress distribution resulting from shrink fitting of the stator of a permanent magnet synchronous motor (PMSM) was computed. From 1-D magnetoelastic characterization data and using von Mises equivalent stress, the local magnetic permeability is defined. The model shows a significant influence of stress on the cogging torque of the PMSM, depending on the frame used for the shrink fitting of the stator. Another early work on this topic was proposed in [2], where the case of a magnetic bearing system was considered.

The stress is induced by centrifugal forces and shrink fitting. It is considered as tensile and introduced as a scalar, both in the definition of reluctivity for the structure model and in the definition of Steinmetz coefficients for the *a posteriori* evaluation of hysteresis losses. However, the simulations show a weak influence of stress.

Later on, several works based on similar approaches were applied to different motor structures, and showed significant effect of stress. In some studies, the modeling results are also supported by experimental evidence. Miyagi *et al.* [3] measured a 28% increase of iron losses due to the stress induced by stator shrink fitting of a surface PMSM (SPMSM) operating at 1000 r/min. The authors managed to predict this increase by computing the distribution of von Mises stress and using *a posteriori* loss evaluation. Yamazaki and Kato [4] evaluated the losses in an interior permanent magnet motor at 2000 and 10 000 r/min. The scalar equivalent stress proposed in [5] is used as an input parameter for the 1-D stress-dependent permeability and for the *a posteriori* losses formulas. It is shown that including the effect of mechanical stress improves the accuracy of the losses estimate. The analysis of modeling results leads to the conclusion that stress induces a 10% increase of both eddy current and hysteresis losses. Zeze *et al.* [6] measured the residual stress on the stator iron sheets of a PMSM. The stress projected along rolling and transverse directions is accounted for in an approximated formulation with complex variables allowing the introduction of losses in the structural analysis. The authors show that the total iron losses evaluated under stress are 80% higher than the losses evaluated without considering the stress. Abdallh and Dupré [7] considered a scalar mechanical stress in the design of an SPMSM based on stress-dependent permeability and *a posteriori* losses formulas. The stress distribution is uniform and does not correspond to any specific loading,

but the results support the fact that stress can have a considerable influence on the motor design. Finally, Xu *et al.* [8] studied a deep-sea SPMSM. The stress state is imposed by stator shrink fitting and by fluid high pressures (due to sea and oil pressure compensation). An experimental setup with fluid pressure control allows the gradual change of the stress source from 0 to 70 MPa. From the experiments, the stress is shown to induce a 40% increase of the iron losses at 6000 r/min. Using a von Mises stress-dependent permeability and an *a posteriori* losses computation by interpolation of measurements under uniaxial loadings, the simulations reproduce the experimental results.

From these few publications dedicated to the evaluation of the influence of mechanical stress on the performance of electrical engineering devices, a few salient points can be highlighted. The devices under scope are motors or motor-like structures with air gap: 1) magnetic bearings [2]; 2) surface permanent magnet [3], [6]–[8]; or 3) interior permanent magnet [4] synchronous motors. The stress sources are shrink fitting, inertial forces, fluid pressure [8], or iron sheet manufacturing processes [6]. The tensor stress distribution is computed by finite elements on the structure. From this, a scalar stress is derived by considering the principal stress (or the highest absolute value among tangential and radial components) [2], the von Mises stress[1] [1], [3], [8], or a magnetoelastic equivalent stress [4]. Only one of these references [6] considered a two-component stress (rolling and transverse direction components), and use an intrinsic approach (losses calculated in the structural analysis). In the others, the structural analysis only takes into account the anhysteretic behavior, and the iron losses are computed *a posteriori*. The effect of stress on the anhysteretic behavior and on the iron losses is obtained from curve fitting from several uniaxial experiments (uniaxial stress parallel to the applied magnetic field).

However, more accurate and predictive material constitutive models could be applied to reach better evaluation and understanding at the structure level. Many models have been developed to represent the hysteretic magnetomechanical behavior of ferromagnetic materials. They are built as the extensions of classical magnetic hysteresis models, such as Preisach [9]–[11] or Jiles–Atherton (JA) models [12], [13], derived from energetic approaches [14]–[16], or based on purely phenomenological descriptions [17]. These models usually handle only uniaxial configurations (uniaxial stress parallel to the applied magnetic field). Uniaxial stress, nonparallel to the magnetic field [15], [18] or biaxial stress [17], [19], are sometimes considered. These models can be applied for the structural analysis of magnetostrictive sensors/actuators in which the stress/field configurations are relatively simple [11], [15], [20]. For the approaches based on classical magnetic hysteresis models, the effect of stress is usually introduced as an additional contribution to the effective magnetic field (i.e., the effective internal field in the magnetization process of domain walls motion and magnetization rotation).

This approach is supported by the experimental observations in uniaxial configuration [21]. In Preisach models, the influence of stress may alternatively be introduced in the distribution function [10].

In this paper, and for the purpose of illustration, we focus on the influence of the stress induced by shrink fitting on the quasi-static hysteresis losses in a switched reluctance motor (SRM) made of initially isotropic nonoriented iron–silicon sheets. Because of the air gap and of the high permeability of the iron–silicon sheets, such a device is mainly induction driven. However, the material is subjected to significant rotating fields, and exhibits hysteresis-induced anisotropy (nonparallel magnetic field and induction). As the material behavior is imposed by the local mechanical stress/magnetic field configuration, a fully multiaxial (vector field and tensor stress) hysteretic approach is sought. The structure analysis being highly demanding in terms of computational burden, a relatively light material constitutive model is needed. We propose here to associate a simplified anhysteretic magnetoelastic multiscale model (SMSM) with an extended vector JA model. Time-stepping finite elements and nonlinear resolution involving the differential permeability tensor are used in order to get the steady state of the quasi-statically rotating SRM (dynamic aspects are overlooked). The analysis of the influence of stress on local and global hysteresis losses is carried out for a given set of feeding current waveforms.

II. MODELING OF MAGNETIC HYSTERESIS UNDER STRESS

A multiscale approach based on the energy balance at the local scale can be a powerful tool to model the complex behavior of the magnetic materials subjected to magnetomechanical loadings. Such an approach has been derived to predict the anhysteretic magnetoelastic behavior under multiaxial configurations [22]. In order to keep reasonable the computational burden, a simplified version (SMSM) is used here. For a given magnetoelastic loading, the predicted anhysteretic magnetization is substituted to the classical Langevin function used in the vector JA model [23]. The average distribution of the magnetic domains, which is an output of the—anhysteretic—SMSM, is also used to make JA's k-parameter stress dependent, allowing a good representation of losses under stress.

A. Anhysteretic Magnetoelastic Simplified Multiscale Model

In order to avoid the computational burden of the full MSM [22], crystallographic texture effects can be neglected, or taken into account only at the macroscopic scale. The material is modeled as a—fictitious—single crystal made of a collection of magnetic domains randomly oriented [24], [25]. At the scale of the magnetic domain, the local magnetization $\vec{M}_\alpha$ and magnetostriction strain $\boldsymbol{\varepsilon}_\alpha^\mu$ depend only on the orientation $\vec{\alpha}$ of the magnetization in the domain and on the saturation magnetization (M_s) and maximum magnetostrictive strain (λ_s). The local potential energy W_α of the material is the sum of magnetic and elastic contributions

$$W_\alpha = -\mu_0 \vec{H} \cdot \vec{M}_\alpha - \boldsymbol{\sigma} : \boldsymbol{\varepsilon}_\alpha^\mu \qquad (1)$$

---

[1]Although it is a questionable choice, since von Mises equivalent stress was designed for plasticity yield detection and does not incorporate any magnetic consideration.

where μ_0 is the vacuum permeability, $\vec{H}$ is the applied magnetic field, and $\boldsymbol{\sigma}$ is the applied stress tensor

$$\vec{M}_\alpha = M_s \, \vec{\alpha}, = M_s \begin{bmatrix} \alpha_1 \\ \alpha_2 \\ \alpha_3 \end{bmatrix} \tag{2}$$

and

$$\boldsymbol{\varepsilon}_\alpha^\mu = \lambda_s \left(\frac{3}{2} \, \vec{\alpha} \otimes \vec{\alpha} - \frac{1}{2} \mathbf{I} \right) \tag{3}$$

with $\mathbf{I}$ the second-order identity tensor. An additional local anisotropy energy could also be considered to represent the macroscopic anisotropy resulting from the combination of crystalline anisotropy and crystallographic texture [24].

An internal parameter f_α is introduced to describe the volume fraction of the set of domains with magnetization orientation $\vec{\alpha}$. The volume fractions are calculated for any $\vec{\alpha}$ using a Boltzmann-type relation [26]

$$f_\alpha = \frac{\exp(-A_s \cdot W_\alpha)}{\int \exp(-A_s \cdot W_\alpha) \, d\alpha} \tag{4}$$

where A_s is a material parameter related to the initial unstressed anhysteretic susceptibility, and the integration is made over the unit sphere considering the differential area $d\alpha$ associated with $\vec{\alpha}$ [25]. The macroscopic anhysteretic magnetization is finally obtained thanks to an averaging operation over all possible directions

$$\vec{M}_{\mathrm{an}}(\vec{H}, \boldsymbol{\sigma}) = \langle \vec{M}_\alpha \rangle = \int f_\alpha \, \vec{M}_\alpha \, d\alpha. \tag{5}$$

The magnetostriction strain can also be calculated in the same way

$$\boldsymbol{\varepsilon}^\mu(\vec{H}, \boldsymbol{\sigma}) = \langle \boldsymbol{\varepsilon}_\alpha^\mu \rangle = \int f_\alpha \, \boldsymbol{\varepsilon}_\alpha^\mu \, d\alpha. \tag{6}$$

The model presented here is close to Armstrong's model [27] except that we consider a larger set of possible domain orientations, and contrary to the model used in [24], we work here with 3-D orientations.

From these equations, the differential magnetic susceptibility tensor can be obtained as (see Appendix A)

$$\boldsymbol{\chi}_{\mathrm{an}} = \frac{\partial \vec{M}_{\mathrm{an}}}{\partial \vec{H}} = \mu_0 A_s \left(M_s^2 \int f_\alpha \vec{\alpha} \otimes \vec{\alpha} \, d\alpha - \vec{M} \otimes \vec{M} \right). \tag{7}$$

All the above-mentioned integrals are numerically evaluated by discrete sums over a set of 2562 almost uniformly distributed possible orientations. Note that for a small set of possible orientations, these integrals can alternatively be calculated analytically [25].

B. Stress-Dependent Vector Jiles–Atherton Model

As mentioned in Section I, stress dependence can be accounted for in the JA model through the use of a specific contribution to the effective field $\vec{H}_e$. Here, we propose another approach taking benefit from the use of the SMSM. The definition of the effective field is kept from the original JA model, depending only on the applied magnetic field

(or alternatively on the applied induction) and on the magnetization state

$$\vec{H}_e = \vec{H} + \beta \vec{M} = \nu_0(\vec{B} + \mu_0(\beta - 1)\vec{M}) \tag{8}$$

where ν_0 is the inverse of the vacuum permeablity and β (classically noted α) accounts for the coupling between magnetic domains. The effect of stress is introduced through the anhysteretic magnetization given by the SMSM applied to this effective field

$$\vec{M}_{\mathrm{an}} = \vec{M}_{\mathrm{an}}(\vec{H}_e, \boldsymbol{\sigma}). \tag{9}$$

The vector extension of JA model [23] is defined by the following implicit nonlinear ordinary differential equation:

$$d\vec{M} = (\vec{\chi}_f \cdot d\vec{H}_e)^+ \vec{u}_{\chi_f} + c \, d\vec{M}_{\mathrm{an}} \tag{10}$$

where $\vec{\chi}_f = (1/k)(\vec{M}_{\mathrm{an}} - \vec{M}) = (1/k)\|\vec{M}_{\mathrm{an}} - \vec{M}\|\vec{u}_{\chi_f}$. The parameter a in the Langevin function for the classical JA definition of $\vec{M}_{\mathrm{an}}$ is related to the A_s parameter of the SMSM used here

$$A_s = \frac{1}{\mu_0 M_s a}. \tag{11}$$

In this model, the parameter k directly acts on the coercive field, and is strongly related to the density of pinning sites and to wall displacements [28]. The effects of mechanical stress on the coercive field and on the loss density have been extensively reported in the literature. Following the interpretation proposed in [29], we assume that the magnitude of wall displacements increases as the volume fraction of domains well oriented with respect to the direction of the magnetization increment decreases. In other words, the losses associated with a magnetization increment are greater if the domains are badly oriented. As the SMSM gives the anhysteretic magnetization and the corresponding distribution of volume fractions, we propose a twofold correction of the unstressed value k_0 for the parameter k

$$k = k_0 \left(1 - \kappa_r \frac{M_{\mathrm{an}}}{M_s} \right) \left(1 + \kappa_f \left(1 - 2 \int f_\alpha |\vec{\alpha} \cdot \vec{m}| \, d\alpha \right) \right) \tag{12}$$

where κ_r and κ_f are constant parameters, and $\vec{m} = \overrightarrow{d\vec{M}}/dM$ represents the direction of the magnetization increment. The first correction term accounts for the fact that the contribution of reversible processes (wall bending or local magnetization rotation) increases as the magnetization increases. This kind of correction was originally introduced in [28]. The second term aims at accounting for the effect of stress through the volume fractions f_α obtained from the SMSM. In the proposed correction, the $(|\vec{\alpha} \cdot \vec{m}|)$ function could be substituted by other convenient functions of the angle $(\vec{\alpha}, \vec{m})$. In the isotropic case considered here, in the absence of applied stress and magnetic field, the distribution of volume fraction is uniform: $f_\alpha = (1/4\pi)$. In consequence: $2 \int f_\alpha |\vec{\alpha} \cdot \vec{m}| \, d\alpha = (1/2\pi) \int |\vec{\alpha} \cdot \vec{m}| \, d\alpha = 1$, and the correction vanishes.

TABLE I

MATERIAL MODEL PARAMETERS

M_s (A.m^{-1})	λ_s	a (A.m^{-1})	c	β	k_0	κ_r	κ_f
1.6 10^6	10^{-5}	50	0.2	10^{-5}	70	0.3	0.3

C. Numerical Evaluation of the JA-SMSM

We define χ_f by the following:

if $\vec{\chi}_f \cdot d\vec{H}_e > 0$

$$\chi_f = |\vec{\chi}_f|^{-1} \, \vec{\chi}_f \otimes \vec{\chi}_f \tag{13}$$

else

$$\chi_f = \mathbf{0}. \tag{14}$$

Then, (10) can be expressed as

$$d\vec{M} = \chi_f d\vec{H}_e + c \, d\vec{M}_{an} \tag{15}$$

or

$$d\vec{M} = (\chi_f + c\chi_{an}(\vec{H}_e, \boldsymbol{\sigma}))(d\vec{H} + \beta d\vec{M}). \tag{16}$$

As shown in [30], the hysteretic differential susceptibility is then

$$\chi = \frac{d\vec{M}}{d\vec{H}} = (\boldsymbol{I} - \beta(\chi_f + c\chi_{an}))^{-1}(\chi_f + c\chi_{an}). \tag{17}$$

Alternatively, we have also

$$\boldsymbol{\xi} = \mu_0 \frac{d\vec{M}}{d\vec{B}} = (\boldsymbol{I} - (\beta - 1)(\chi_f + c\chi_{an}))^{-1}(\chi_f + c\chi_{an}). \tag{18}$$

For a given applied magnetic field or induction, the magnetization can then be computed by a simple Euler forward difference scheme

$$\vec{M}^{i+1} = \vec{M}^i + \frac{d\vec{M}}{d\vec{H}}(\vec{M}^i, \vec{H}^i)(\vec{H}^{i+1} - \vec{H}^i) \tag{19}$$

$$\vec{M}^{i+1} = \vec{M}^i + \frac{d\vec{M}}{d\vec{B}}(\vec{M}^i, \vec{B}^i)(\vec{B}^{i+1} - \vec{B}^i) \tag{20}$$

where the superscript i indicates the time step.

The values of the parameters used in this paper are given in Table I. These values are chosen to reproduce the typical behavior of iron silicon nonoriented steel sheets used in electrical motors. No specific material is defined, and the properties are assumed to be isotropic. In consequence, typical values of the J–A coefficients are chosen from the values found in different references, such as [31]–[35], considering either the rolling or the transverse direction. Measurements of the hysteretic magnetomechanical behavior can be found in the literature, and show, for example, the variations of the losses or of the hysteresis loops under uniaxial stress for alternating [36], [37] and rotating [38] magnetic loading. The measurement of losses under biaxial stress have also been proposed recently [39]. The correction parameters for k are chosen as $\kappa_f = 0.3$ and $\kappa_r = 0.3$. The influence of these parameters on the shape of the hysteresis loops and on the hysteresis losses is shown in Appendix B. Parameter κ_r is chosen in order to qualitatively reproduce the variation of the shape of the loops (wider for low fields),
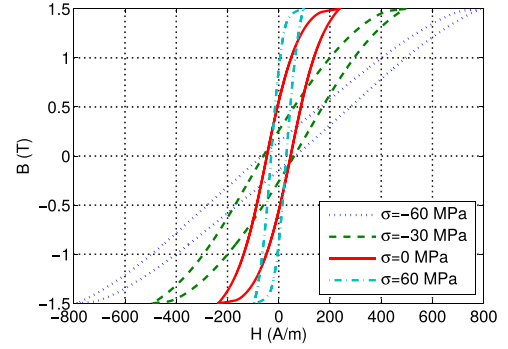
Fig. 1. Uniaxial stress-dependent hysteresis loops for $B_{max} = 1.5$ T, with material parameters from Table I.
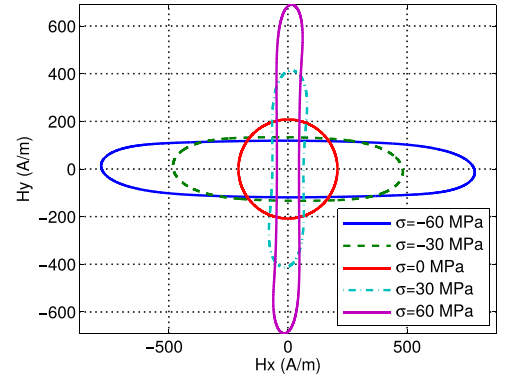
Fig. 2. Locus of $\vec{H}$ for a rotational induction with $B = 1.5$ T and various uniaxial stress levels (stress oriented along x-direction). Material parameters from Table I.

and parameter $\kappa_f = 0.3$ is tuned to capture the variation of the density of hysteresis losses under uniaxial stress. The model parameters have not been the object of a specific identification procedure. The existing advanced procedures [31]–[35], [40]–[43] for JA classical model parameter identification could be applied using characterization data without stress. These procedures could also be extended to include κ_r and κ_f, considering at least characterization data under uniaxial magnetomechanical loading.

Hysteresis loops under applied alternating induction [max(B_x) = 1.5 T and $B_y = B_z = 0$] and $\vec{H}$-loci under applied circular induction ($B = 1.5$ T) are presented in Figs. 1 and 2 for a uniaxial stress loading ($\sigma_{xx} = \sigma$ and $\sigma_{yy} = \sigma_{xy} = 0$). The stress σ is chosen in the range (from -60 to 60 MPa): negative values correspond to compressive stress, and positive values correspond to tensile stress. Under alternating induction (Fig. 1), the shape of the loop is strongly modified by the stress: permeability increases and coercive field decreases when the stress increases. Under circular induction (Fig. 2), a stress-induced anisotropy clearly appears. Since an (initially) isotropic material is considered, the locus is circular when no stress is applied. The stress dependence of hysteresis losses is evaluated for the same applied alternating or circular induction considering different tensor forms: 1) uniaxial stress ($\sigma_{xx} = \sigma$ and $\sigma_{yy} = \sigma_{xy} = 0$); 2) equibiaxial stress ($\sigma_{xx} = \sigma_{yy} = \sigma$ and $\sigma_{xy} = 0$); and 3) pure shear stress ($\sigma_{xx} = \sigma_{yy} = 0$ and $\sigma_{xy} = \sigma/2$). Fig. 3 shows that losses are more sensitive to stress under
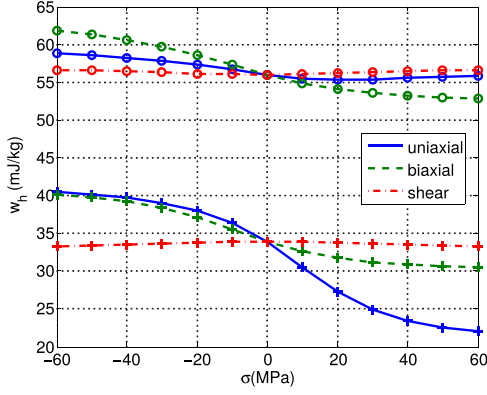
Fig. 3. Hysteresis losses as a function of the uniaxial, biaxial, or shear stress for alternating (+) and circular (o) applied induction ($B_{\max} = 1.5$ T and material parameters from Table I).

alternating induction (+) than under circular (o) induction loading. The effect of the shear stress (σ_{xy}) is relatively weak. The effect of stress amplitude is not symmetrical with respect to $\sigma = 0$. The evolution of losses with stress can even be nonmonotonic (see the uniaxial configuration for a circular induction).

III. SOLUTION OF THE STRUCTURAL MAGNETOSTATIC AND MECHANICAL PROBLEMS

A. Magnetostatic Problem: Time-Stepping Finite-Element Method

The problem to solve is a 2-D magnetostatic configuration involving magnetic materials and imposed source current density ($\vec{J}$). The hysteretic magnetic behavior of the material is given by the model presented Section II, and depends on the local value of an imposed mechanical stress field. A time-stepping finite-element method is chosen. At each time step, a nonlinear single-valued behavior can be considered for the material. Both scalar potential [including a source vector potential $\vec{T}$, such as curl $(\vec{T}) = \vec{J}$] and vector potential formulations are available because the material model can handle either $\vec{H}$ (direct fashion) or $\vec{B}$ (inverse fashion) as input parameter. However, our numerical experiments show that the scalar potential formulation exhibits significantly worse convergence properties for our application, and only the vector potential formulation is detailed here.

1) Finite-Element Formulation: The magnetic vector potential is written as

$$\vec{A} = \sum_{i=1}^{N} \boldsymbol{A}_n \cdot \vec{w}_n \tag{21}$$

where N is the number of mesh nodes, $\boldsymbol{A}_n$ is the degree of freedom, and $\vec{w}_n = w_n \vec{z}$ is the nodal linear interpolation function. The Galerkin weak form is derived from the Maxwell–Ampère relation: for any $n \in [1, N]$

$$F_n(\boldsymbol{A}) = (\text{curl } \vec{H} - \vec{J}, \vec{w}_n)_\Omega = 0 \tag{22}$$

where the material behavior is given by $\vec{H} = v_0 \vec{B} - \vec{M}$, and the Maxwell–Thomson relation is satisfied by defining $\vec{B} = \text{curl } \vec{A}$. $\boldsymbol{A}$ is the column vector containing the degrees of freedom and $\vec{J}$ is the imposed current density at the considered

step. The condition $\vec{n} \times \vec{A} = \vec{0}$ is considered at the outer boundary of the study domain (Ω). This nonlinear system of equations is solved at each time step.

2) Newton–Raphson Method: The Newton–Raphson (NR) method consists in solving iteratively the problem as given by the first-order Taylor approximation of (22): for any $n \in [1, N]$

$$F_n^{j-1} + \left(\frac{dF_n}{d\boldsymbol{A}}\right)^{j-1} (\boldsymbol{A}^j - \boldsymbol{A}^{j-1}) = 0 \tag{23}$$

where $(dF_n/d\boldsymbol{A})$ is the raw vector defined by its components

$$\frac{\partial F_n}{\partial \boldsymbol{A}_m} = \left(\text{curl } \frac{\partial \vec{H}}{\partial \boldsymbol{A}_m}, \vec{w}_n\right)_\Omega. \tag{24}$$

Then, using the chain rule [44]

$$\frac{\partial \vec{H}}{\partial \boldsymbol{A}_m} = \frac{\partial \vec{H}}{\partial \vec{B}} \frac{\partial \vec{B}}{\partial \boldsymbol{A}_m} = \boldsymbol{v}_d \text{ curl } \vec{w}_m \tag{25}$$

where $\boldsymbol{v}_d = (\partial \vec{H}/\partial \vec{B}) = v_0(1 - \boldsymbol{\xi})$ and $\boldsymbol{\xi}$ is defined by (18). The system defined by (22) is hence solved iteratively considering

$$\vec{H}^j = \boldsymbol{v}_d^{j-1}(\vec{B}^j - \vec{B}^{j-1}) + \vec{H}^{j-1}. \tag{26}$$

Initializing $\vec{H}^0$, $\boldsymbol{v}_d^0$, and $\vec{B}^0$ from the solution at the former time step, the first iteration of the NR method gives the solution of the fully linearized problem.

3) Fixed Point Method With Local Coefficient: An alternative to solve the nonlinear problem is the fixed point method in which the magnetic field is expressed as: $\vec{H} = \boldsymbol{v}\vec{B} - \vec{\mathcal{M}}$, where $\boldsymbol{v}$ is chosen so as to ensure the convergence [45]. Then, the system defined by (22) is solved iteratively considering

$$\vec{H}^j = \boldsymbol{v}\vec{B}^j - \vec{\mathcal{M}}^{j-1} = \boldsymbol{v}(\vec{B}^j - \vec{B}^{j-1}) + \vec{H}^{j-1}. \tag{27}$$

Following the local coefficient approach [46] but considering a tensor fixed point parameter $\boldsymbol{v}$, we define locally (in space and time)

$$\boldsymbol{v} = C\boldsymbol{v}_d^0 \tag{28}$$

where $C > 1$ is a scalar coefficient and typically $1 < C < 2$. The fixed point iteration can be started from the solution of the fully linearized problem described above.

4) Convergence Criterion and Nonlinear Constitutive Law: For both of these iterative methods, the convergence criterion is defined from the l^2 norm of the residual

$$||F^j|| < c_c. \tag{29}$$

At each nonlinear iteration, the magnetization state ($\vec{M}^j$ and $\boldsymbol{\xi}^j$) is computed for $\vec{B}^j$ and from the magnetization state at the former time step, subdividing the variation of induction ($\vec{B}^j - \vec{B}^0$) in order to apply the Euler scheme given by (20). The number of substeps is typically $n_{ss} = 3$, but integration inaccuracies are avoided by defining a maximum variation of magnetization ($\delta M_{\max} = 0.01 M_s$), and finally

$$n_{ss} = \max\left(3, \text{ceil}\left(\frac{||v_0(\vec{B}^j - \vec{B}^0)\boldsymbol{\xi}^0||}{\delta M_{\max}}\right)\right). \tag{30}$$

Considering that the condition $\vec{\chi}_f \cdot d\vec{H}_e > 0$ is evaluated from the former time step, this process defines the single valued (nonhysteretic) magnetic behavior.
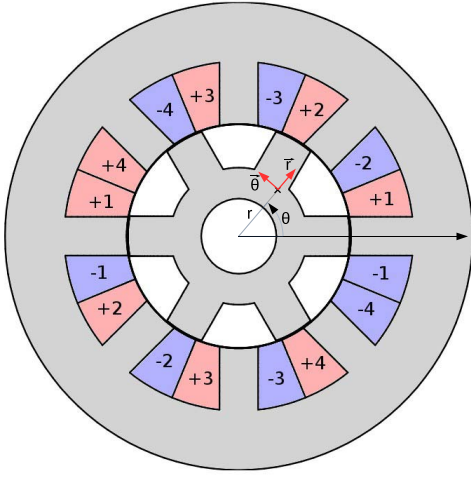
Fig. 4. SRM geometry with coordinate system and phase numbering definitions.

TABLE II

SRM Geometric Parameters

	Rotor	Stator
Inner radius (cm)	1.15	3.43
Outer radius (cm)	3.39	7.15

B. Static Linear Elasticity Problem

The stress distribution is given by the solution of the static linear elasticity small displacement problem. The formulation in terms of mechanical displacement ($\vec{u}$) is presented here including the force density ($\vec{f}$) and considering a possible effect of the magnetostriction strain ($\boldsymbol{\varepsilon}^{\mu}$). The linear relation between the stress ($\boldsymbol{\sigma}$) and the elastic strain ($\boldsymbol{\varepsilon}^e$) then reads

$$\boldsymbol{\sigma} = \boldsymbol{C} : \boldsymbol{\varepsilon}^e = \boldsymbol{C} : (\boldsymbol{\varepsilon} - \boldsymbol{\varepsilon}^{\mu}) \tag{31}$$

where $\boldsymbol{C}$ is the elasticity tensor and $\boldsymbol{\varepsilon}$ is the total strain. The equation to be solved is

$$\mathrm{div}\,(\boldsymbol{\sigma}) = -\vec{f} \tag{32}$$

with the strain-displacement relation

$$\boldsymbol{\varepsilon} = \mathrm{grad}_s\,\vec{u} \tag{33}$$

and with boundary conditions. The stress distribution is computed once for all before starting the time-stepping solution of the magnetostatic problem considering $\vec{f} = \vec{0}$ and $\boldsymbol{\varepsilon}^{\mu} = 0$.

IV. Application to a Switched Reluctance Motor

The 8/6 SRM under study is presented in Fig. 4 in the reference configuration (relative position of the rotor and the stator). The outermost radius of the stator is $R_s = 7.15$ cm, the outermost radius of the rotor is $R_r = 3.39$ cm, and the air-gap width between the teeth is $g = 0.4$ mm (Table II). We consider two systems of polar coordinates (r, θ), each one being attached to the direction of a reference tooth of the rotor or the stator. The same notation is used for both the systems. The finite-element problems are solved using FreeFem++ [47] including the SMSM as a dynamically linked and parallelized function.

(a)

(b)

(c)
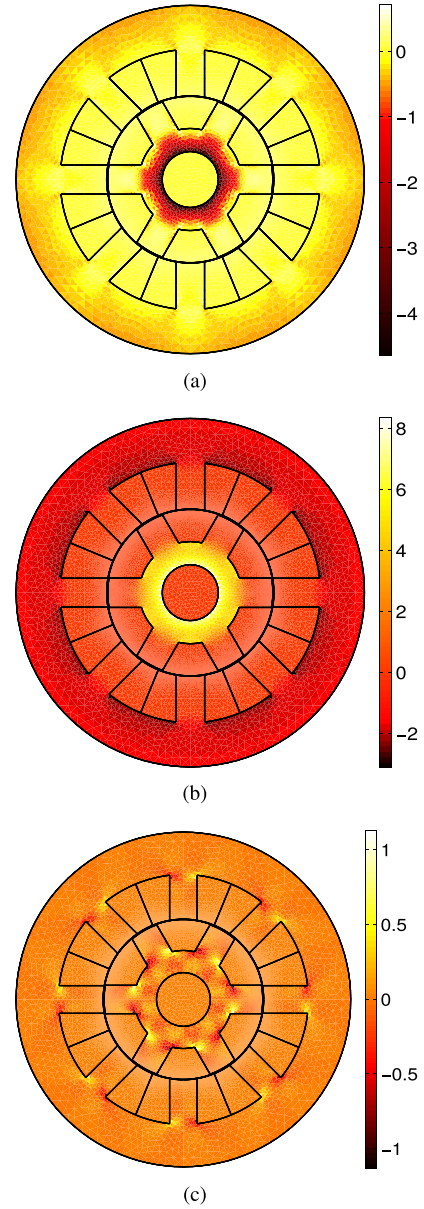
Fig. 5. Distribution of the stress induced by shrink fitting (megapascal) for an imposed radial displacement of $|\delta R| = 0.5$ μm. (a) σ_{rr}. (b) $\sigma_{\theta\theta}$. (c) $\sigma_{r\theta}$.

A. Stress Distribution

The stator and the rotor are considered to be made of the same nonoriented iron sheets. The mechanical stress is induced by shrink fitting of the outer frame (not represented here) on the stator and of the shaft on the rotor. The effect of shrink fitting is accounted for by imposing a constant radial displacement on the shaft/rotor ($\delta R = 0.5$ μm) and the frame/stator ($\delta R = -0.5$ μm) interfaces. The other boundaries are assumed to be free to move ($\boldsymbol{\sigma} \cdot \vec{n} = \vec{0}$). The problem is solved by the finite-element method with the first-order nodal interpolation functions for each component of the displacement, considering the plane stress approximation and isotropic elastic properties (Young's modulus $E = 210$ GPa and Poisson's ratio $\nu = 0.29$). The corresponding stress distribution is shown in Fig. 5(a)–(c). In most of the motor, the stress is biaxial with principal axes $\vec{\theta}$ and $\vec{r}$. The shear component $\sigma_{r\theta}$ is very small all
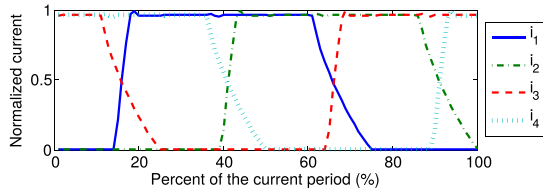
Fig. 6. Waveforms of the current in all phases.

(a)

(b)
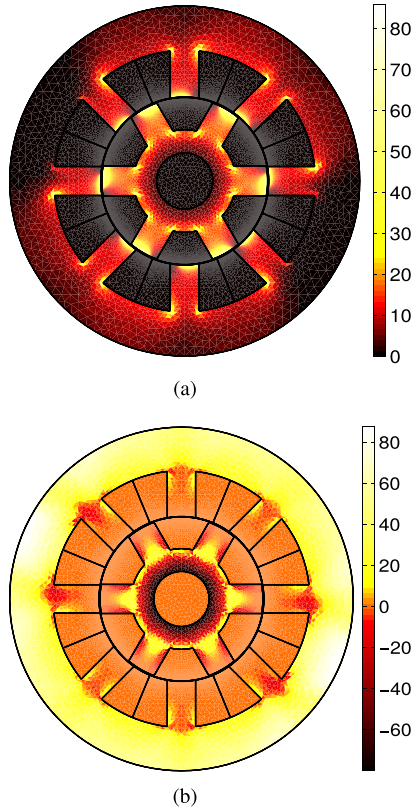
Fig. 7. Distribution of the density of hysteresis losses and effect of stress. (a) Density of hysteresis losses for $5\delta R$ (mJ/kg). (b) Relative difference (%) between the densities of hysteresis losses for $5\delta R$ and $0\delta R$.

over the structure apart from the localized regions near sharp geometric angles. The teeth of the structure are stress free. In the central part of the rotor, the maximum principal stress is tensile along the direction $\vec{\theta}$ ($\sigma_{\theta\theta} \approx 6$ MPa). In the stator, the maximum principal stress is compressive along the direction $\vec{\theta}$ ($\sigma_{\theta\theta} \approx -2$ MPa). These results were checked by comparison with the ones obtained using higher order (two or three) interpolation functions for the displacement to discard a possible overestimation of the stress level due to the first-order approximation.

In the analysis of magnetic hysteresis losses, we considered shrink-fitting displacements ranging from 0 (no stress) to 5 times δR. As the elasticity problem is linear, the stress induced by a shrink fitting with $|N\delta R|$ is N times greater than the one presented here. The influence of magnetostriction and magnetic forces on the stress distribution is neglected. Appendix C provides the justification for this assumption.

B. Hysteresis Losses

The shaft and the frame are assumed to be nonmagnetic. The regions where the source currents are applied are shown

in Fig. 4, with the corresponding phase numbers and a sign indicating the orientation of the current. The motor angular position (θ_R) is defined by the angle between the reference teeth of the rotor and the stator. For each phase, a typical period of the current waveform [48] is given in Fig. 6 and is sampled to get 200 time steps. The initial position of the rotor corresponds to $\theta_R = -42.6°$. In order to allow the rotation, a moving band is used in the finite-element model. A narrow circular band in the air gap is remeshed at each step. This band does not contain any inner mesh node, which means that only the connection between the existing mesh nodes is actually updated at each step. Starting from the unmagnetized state, a ten time-step magnetization is carried out in the initial position to reach the initial values of the current in each phase. Afterward, two 360° rotations are simulated. Considering that the steady state is reached, the last 360° rotation gives the full cycle of the magnetic state at any location in the SRM. In the stator, this full cycle corresponds in fact to six periods for the local fields (phase current period). At each of the $(10 + 2 \times 6 \times 200) = 2410$ time steps, the nonlinear problem is solved considering the convergence criterion with $c_c = 10^{-2}$ A. For this value, our numerical experiments show that for the fixed point method with local coefficient, the convergence is too slow to obtain the results in a reasonable time. The results presented here are obtained with the NR method, which typically converges within one to four iterations. The mesh is composed of 37 212 nodes and 74 306 triangular elements. One full simulation lasts ~5 h on a 3.3 GHz computer with eight cores (the loop on the elements of the mesh for the evaluation of the SMSM is parallelized using OpenMP library). The values of source current chosen here lead to a maximum induction of 0.55 T in the middle of a stator tooth. For higher values of current, the simulation faces convergence issues (NR method diverges and fixed point method may converge but too slowly). Some considerations about the convergence and stability of the proposed scheme are given in Appendix D.

The analysis of local hysteresis loops and/or induction loci is presented in Appendix E. In this section, we focus on the analysis of the density and the global value of the hysteresis losses. The density of hysteresis losses is computed by the numerical evaluation of the following integral over the last full cycle:

$$w_h = \oint \vec{H} d\vec{B}. \tag{34}$$

The distribution of the hysteresis losses density is given in Fig. 7(a) for a stress corresponding to $5\delta R$. The relative difference with respect to the unstressed case ($0\delta R$) is also presented [Fig. 7(b)]. It can be noticed that the highest values of hysteresis losses density are reached close to sharp angles and in narrow regions at the end of the teeth. In the latter, the considered mechanical stress has merely no influence. However, in the other regions, the stress has a strong effect, and causes locally from -70% to 80% variations, even if the stress remains relatively small (all components are below 45 MPa for the $5\delta R$ shrink fitting). The overall losses over a period (360°) for the stator and the rotor in the unstressed
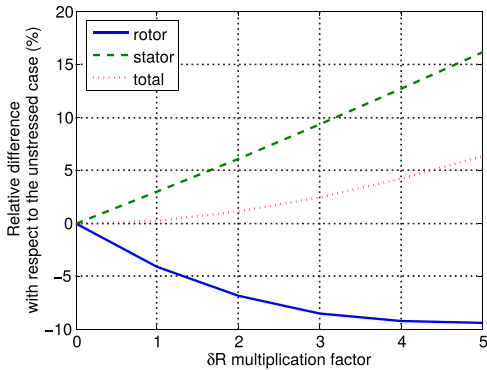
Fig. 8. Sensitivity of the global hysteresis losses to shrink fitting.

configuration are 55.1 and 34.5 mJ, respectively. The effect of stress on these global losses is presented in Fig. 8. It is evident that shrink fitting has significant and opposite effects on losses in the rotor (up to 10% decrease) and in the stator (up to 15% increase). This effect should saturate for higher stress levels.

V. Conclusion

Electrical iron alloys exhibit coupled magnetomechanical behavior. Mechanical stress can have a significant effect on the performance of electrical engineering devices. In order to better understand and quantify this effect, appropriate material constitutive model is needed. These models must be predictive but remain affordable in terms of numerical evaluation. The predictive skills are crucial to be able to consider the variety of mechanical stress/magnetic field configurations that may arise in the structure. The computational burden must be sufficiently low to enable the simulation of complex structures.

In this paper, a material constitutive model is proposed, taking benefit from the predictive skills of a previously published multiscale approach, and introducing the effect of multiaxial stress through the anhysteretic magnetization and the pinning parameter of the vector JA model. The simplified multiscale approach relies only on few material parameters and provides a description of the coupled magnetomechanical anhysteretic behavior. In JA model, the anhysteretic behavior appears as an input parameter, and the so-called pinning parameter k is strongly related to the coercive field. This is why this model of magnetic hysteresis is used as a basis here. However, JA approach is known to suffer from the lack of physical meaning of its parameters [49], from its inaccuracy in the representation of minor loops and from its weakness in the description of dynamic hysteresis. To overcome these limitations, other approaches capable of introducing hysteresis effects within the multiscale model [50] might be considered in the future.

The finite-element analysis is carried out using a time-stepping scheme with nonlinear iteration. The evaluation of the differential susceptibility from the material model allows using the NR method or the fixed point method with local coefficient. In this paper, there is no precise rule to ensure the convergence conditions. In particular, for the fixed point method, the local coefficient is chosen from numerical experiments, because the research interval is not known *a priori* and then the

bounds of the differential susceptibility cannot be computed. For the NR method, besides the usual convergence difficulties, inflection points that may appear from the behavior model can provoke divergence. More robust nonlinear solvers [51] should be implemented in order to consider a wider range of material parameters and higher values of input currents. Methods used in structural mechanics involving hysteretic materials, such as the return mapping algorithm [52], could also offer an alternative to overcome the convergence difficulties. Moreover, the time-stepping scheme could be substituted by an harmonic balance analysis to get directly the steady state of the studied device [53], [54]. This method would allow the parallelization of the finite-element solution of the uncoupled harmonics at each nonlinear iteration step. The material model could also be evaluated in a more efficient way as the whole cycle in each element would be computed at once. This method was recently applied to the simulation of a 3-D structure with hysteretic media [55], and appears to be a powerful alternative.

If the intrinsic approach (hysteresis model inside finite element method) used here may not be implementable in any commercial simulation tools, *a posteriori* approaches may be adopted. In particular, the waveforms of the induction can be reasonably computed using the anhysteretic model, and recorded on the whole system for one time period. Then, using these induction waveforms as the input of the hysteretic model, losses can be evaluated (an example is shown in Appendix F in the no-stress case). However, the ability of such *a posteriori* approaches to capture the effect of stress on losses is still to be assessed.

The SRM test configuration shows that the stress induced by shrink fitting, although moderate in magnitude, has significant effect on hysteresis losses. Different shrink-fitting intensities are considered in order to cover a realistic range. From the knowledge of the frame and shaft material and from the temperatures associated with the shrink-fitting process, the stress distribution could be accounted for more accurately. However, it is believed that this stress would not differ significantly from the one determined here.

The effect of stress could also appear on other global quantities such as the motor torque, in particular for motors exhibiting relatively high iron losses or with a smaller air gap.

Finally, specific experimental setups should be tailored in order to validate simulations at the structure level. The proposed SRM study constitutes a realistic configuration but is difficult to reproduce experimentally: it implies the control of the phase currents, the rotor position, and, more complicated, a set of SRMs with different shrink-fitting conditions (but the same material characteristics). The proposed modeling tool, however, is versatile enough to be adapted to different motor architectures.

Appendix A
Calculation of the Anhysteretic Differential Susceptibility

The differential magnetic susceptibility χ_{an} used in the modeling is given by (7). The corresponding calculation is

presented hereafter. From (5) and because the directions $\vec{\alpha}$ do not depend on the magnetic field, we can write

$$\frac{\partial \vec{M}_{an}}{\partial \vec{H}} = \int \frac{\partial f_\alpha}{\partial \vec{H}} \otimes \vec{M}_\alpha \, d\alpha. \tag{35}$$

We define

$$g_\alpha = \exp(-A_s \cdot W_\alpha) \tag{36}$$

so that

$$f_\alpha = \frac{g_\alpha}{\int g_\alpha \, d\alpha}. \tag{37}$$

Then, we have

$$\frac{\partial f_\alpha}{\partial \vec{H}} = \frac{\partial g_\alpha}{\partial \vec{H}} \frac{1}{\int g_\alpha d\alpha} + g_\alpha \frac{-1}{(\int g_\alpha d\alpha)^2} \int \frac{\partial g_\alpha}{\partial \vec{H}} d\alpha. \tag{38}$$

Considering the expression of W_α given by (1)

$$\frac{\partial g_\alpha}{\partial \vec{H}} = -A_s \frac{\partial W_\alpha}{\partial \vec{H}} \exp(-A_s \cdot W_\alpha) = \mu_0 A_s g_\alpha \vec{M}_\alpha. \tag{39}$$

Combining (38) and (39), we obtain

$$\frac{\partial f_\alpha}{\partial \vec{H}} = \mu_0 A_s f_\alpha (\vec{M}_\alpha - \vec{M}). \tag{40}$$

Finally, introducing this latest result into (35), we find the expression given by (7).

Appendix B
Influence of Parameters κ_r and κ_f

The magnetization and stress-dependent parameter k allow fitting the shape of the hysteresis loop and reproducing the losses behavior. In the proposed evolution of JA vector model, the parameter is defined as a function of two additional parameters, κ_r and κ_f (12). The role of these two parameters is illustrated in this appendix considering a uniaxial stress loading.

Under alternating induction, parameter κ_r can be used to tune the variation of the width of the cycle with the level of magnetization (Fig. 9). Fig. 10(a) and (b) shows the variation of the coercive field (H_c) and of the remanent magnetic induction (B_r) as the functions of the uniaxial stress magnitude for different values of κ_f (with $\kappa_r = 0.3$). For $\sigma = 0$, H_c and B_r hardly depend on κ_f so that they remain as relevant data for the identification of the other parameters of the hysteresis model from unstressed experimental results. Parameter κ_f allows the control of the losses dependence on the stress (Fig. 11) and can be chosen in order to get the desired amplitude of losses variation. It can be noticed that for $\kappa_f = 0$ (i.e., k stress independent), hysteresis losses decrease when the stress increases, because of the stress-dependent anhysteretic magnetization.

Under rotating induction ($B = 1.5$ T), the effect of parameter κ_f on hysteresis losses is shown in Fig. 12. For such a level of induction, an increasing parameter κ_f induces a global increase of losses and sharpens the variations with respect to stress.
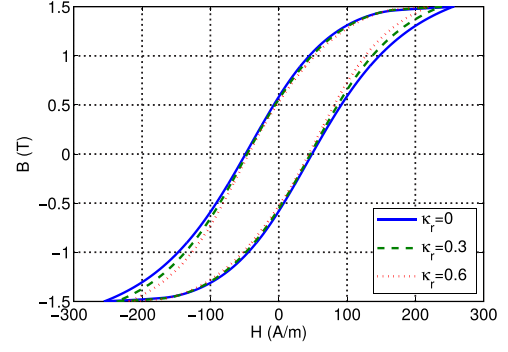
Fig. 9. Role of parameter κ_r on the shape of the hysteresis loop ($\kappa_f = 0$, $B_{max} = 1.5$ T, and other parameters from Table I).

(a)

(b)
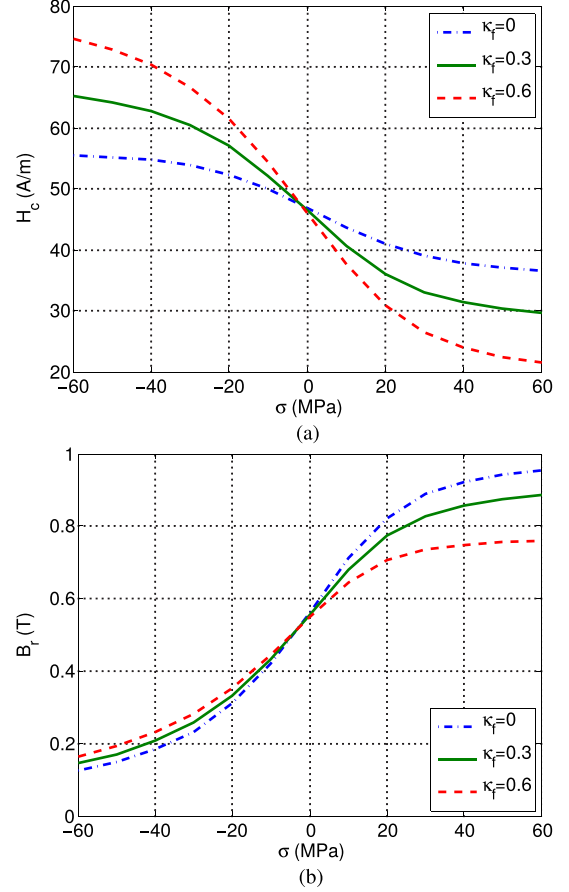
Fig. 10. Role of parameter κ_f on the stress-dependent magnetic response under uniaxial configuration ($B_{max} = 1.5$ T and material parameters from Table I). (a) Coercive field. (b) Remanent induction.

Appendix C
Stress Induced by Magnetostriction and Magnetic Forces

The finite-element computation presented in Section IV is performed neglecting magnetostriction and magnetic forces. The justification is given hereafter by estimating the mechanical stress induced by magnetostriction and by magnetic forces separately. For that purpose, we restrict the study to the anhysteretic case. The reason for this restriction is on one hand (for magnetostriction) the model presented in Section II does
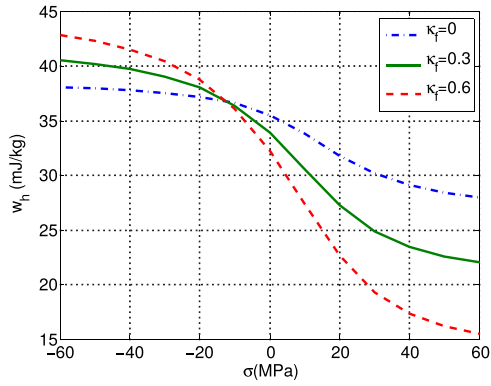
Fig. 11. Stress dependence of magnetic hysteresis losses and influence of parameter κ_f for a uniaxial configuration ($B_{\max} = 1.5$ T and material parameters from Table I).
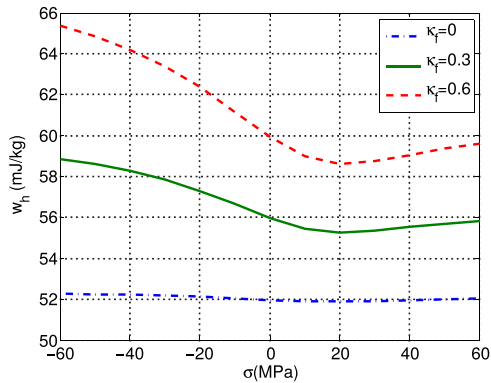
Fig. 12. Effect of parameter κ_f on the variation of the hysteresis rotating losses under stress ($B = 1.5$ T and material parameters from Table I).
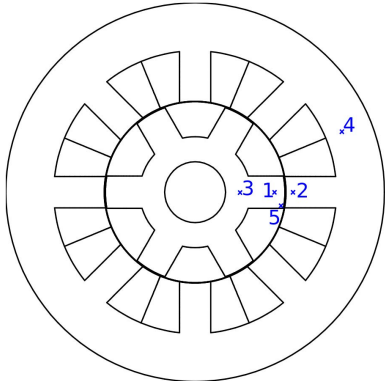
Fig. 13. Location and index of the studied points in the SRM.

not explicitly provide the hysteretic magnetostriction strain, and on the other hand (for magnetic forces) the model does not allow the evaluation of the proportion of energy stored in the material versus losses instantaneously. The anhysteretic case is obtained by changing the value of two parameters: 1) $k = 10^{30}$ and 2) $c = 1$. In the following computations, there is no stress induced by shrink fitting, and the shaft/rotor and the stator/frame interfaces are under no-displacement boundary conditions.

Magnetic forces are computed using the virtual power principle neglecting magnetostriction. The anhysteretic magnetostriction strain is given by the SMSM. The
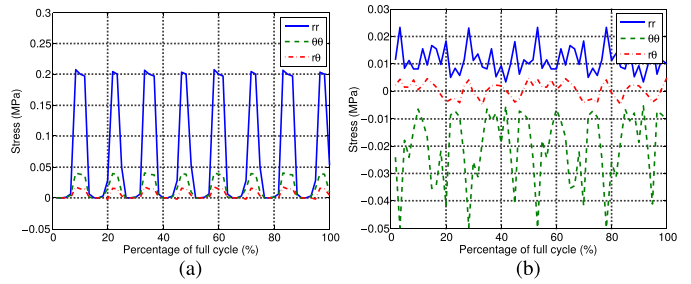
Fig. 14. Component of the stress tensor σ induced by magnetic forces and by magnetostriction. (a) Magnetic forces (at point 5). (b) Magnetostriction (at point 3).
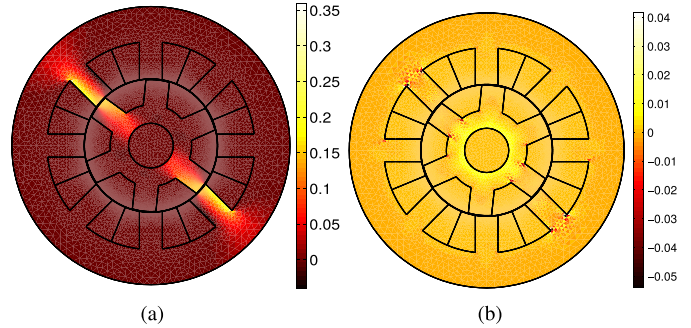
Fig. 15. σ_{rr} (megapascal) induced by magnetic forces and by magnetostriction. (a) Magnetic forces. (a) Magnetostriction.

corresponding stress distributions are computed at each time step. The evolution of all the components of the induced stress is presented in Fig. 14 for a full cycle at point 5 for magnetic forces and point 3 for magnetostriction. For a time step corresponding almost to the maximum value of the stress induced by magnetic forces, the distribution on the SRM is presented in Figs. 15–17. It is shown from these distributions that the stress induced by magnetic forces is greater than the stress induced by magnetostriction and that both would have negligible effect on the magnetic behavior. It can be noticed that the distribution of the stress induced by magnetostriction is not very smooth especially near the sharp angles of the geometry. In fact, magnetostriction is imposed by the magnetic field, and presents strong variations in these regions. The mesh used in these computations is hardly fine enough to represent these variations, and as a consequence, the expected periodic pattern of the stress is difficult to capture (Fig. 14).

APPENDIX D
CONVERGENCE AND STABILITY

For the chosen time step and source current value, NR process converges within one to four iterations (the mean value of the number of iterations over the whole simulation time is 2.15). Considering the fully linearized (FL) approach, the same results can be obtained by reducing the time step. As an example, we present the hysteresis loops at point 5 (Fig. 13), where the fields are mainly radial (Fig. 18). It is shown that for the chosen time step, the NR method and the FL approach give different results. However, choosing a four-times smaller time step, the FL approach gives an hysteresis loop very close
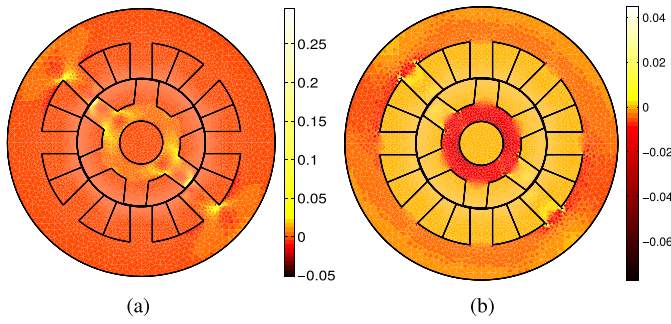
Fig. 16. σ_{tt} (megapascal) induced by magnetic forces and by magnetostriction. (a) Magnetic forces. (b) Magnetostriction.
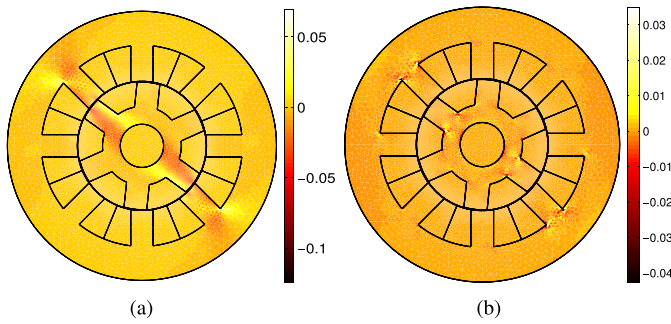
Fig. 17. σ_{rt} (megapascal) induced by magnetic forces and by magnetostriction. (a) Magnetic forces. (b) Magnetostriction.
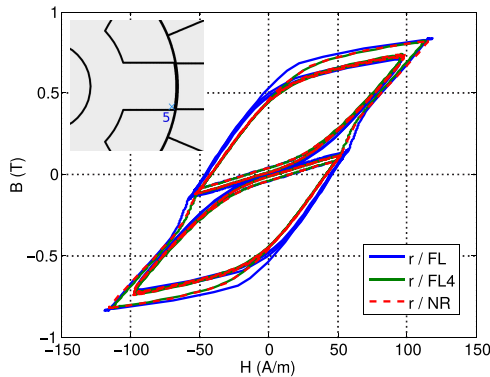
Fig. 18. Hysteresis loop (r-component) at point 5, and comparison between different numerical solutions.

to the one obtained using the NR method. For higher value of input current (1.5 or 2 times greater), we observe that NR process does not converge (divergence may appear during the first magnetization) and the FL approach exhibits unstability (nonperiodical and possibly divergent solution). In this case, the fixed-point method with local coefficient could be used, but it might lead to unaffordable simulation time.

APPENDIX E
LOCAL HYSTERESIS LOOPS

The induction and the magnetic field are recorded at different points in the SRM (Fig. 13) and are analyzed for stress loadings corresponding to $0\delta R$ and $5\delta R$. In the teeth of the rotor and the stator (points 1 and 2), the local stress is very small and the global effect of stress is not significant
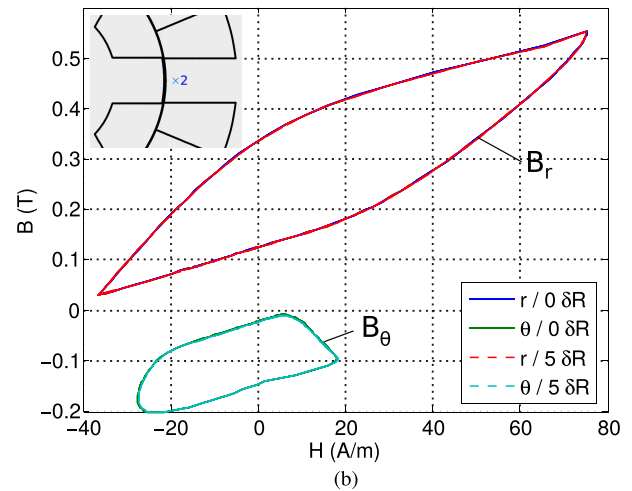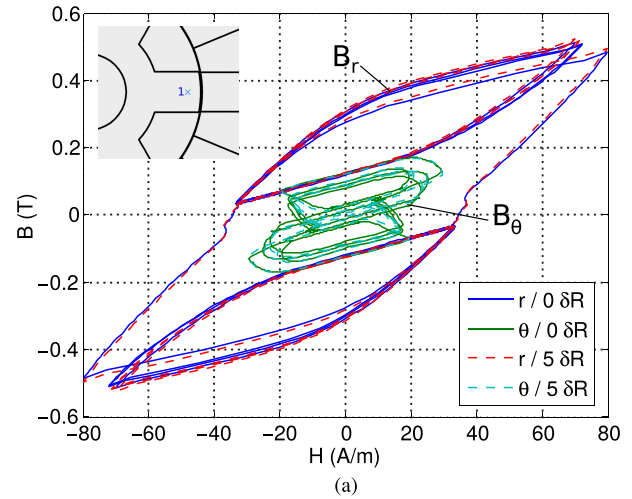
Fig. 19. Hysteresis loops in the teeth (r-component and θ-component). (a) Point 1. (b) Point 2.

[Fig. 19(a) and (b)]. Induction and field slightly rotate but remain mainly radial. At point 1 (in the rotor), the full cycle exhibits a major loop and 2 times four dc-biased minor loops, because this point sees four successive phases with the same orientation and then an orientation switch during the transition between phases 1 and 4. At point 2 (in the stator), the full cycle is composed of six dc-biased superimposed minor loops. In the basis of a rotor tooth (point 3), the effect of stress is significant [Fig. 20(a)], and the fields strongly rotate [Fig. 20(b)]. It can be noticed that the induction is strengthened in direction θ, corresponding to the local tensile stress. At point 4 (in the stator) [Fig. 21], the fields lie almost along direction θ and the compressive stress increases the variations of the magnetic field but does not have a significant effect on the maximum values of the induction.

APPENDIX F
A Posteriori EVALUATION OF LOSSES

Because of the air gap of the SRM, the distribution of induction is not very sensitive to the effective permeability of iron (nonsaturated). In consequence, at any point of the SRM, the waveforms of the induction might be computed using the anhysteretic model. Then, losses can be evaluated

(a)

(b)
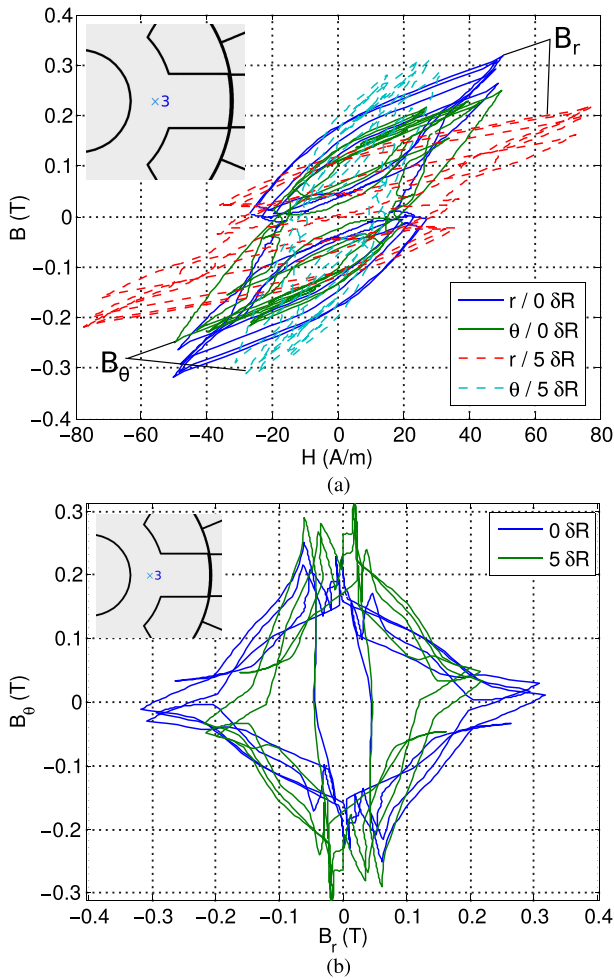
Fig. 20. Hysteresis loops (r-component and θ-component) and B locus at point 3. (a) Hysteresis loop. (b) B locus.
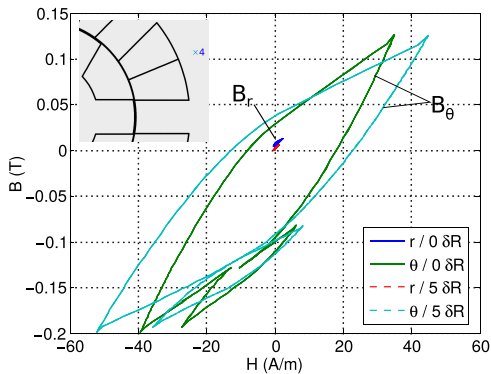
Fig. 21. Hysteresis loops (r-component and θ-component) at point 4.

a posteriori using this induction as the input of the hysteretic model. Such an approach was applied in the no-stress case. Fig. 22 shows the hysteresis loops for the radial components obtained from the *a posteriori* and intrinsic approaches. It can be noticed that the maximum values of magnetic field and induction significantly differ. Fig. 23 shows the relative difference between the losses evaluated from the two approaches. This relative difference can reach 50% in the regions with low density of losses and 20%–30% at the end of the teeth
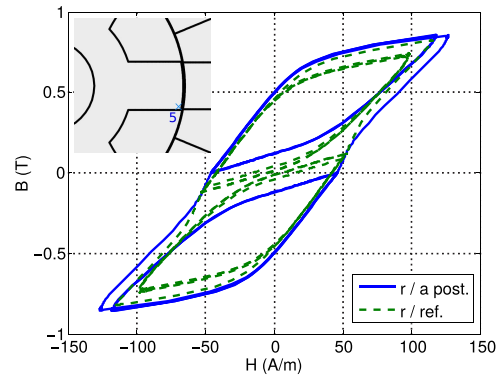
Fig. 22. Hysteresis loop for the radial component at point 5, *a posteriori* and intrinsic (reference) approaches.
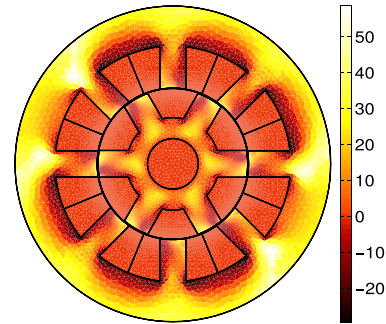
Fig. 23. Density of hysteresis losses, and relative difference between *a posteriori* and intrinsic (reference) approaches (%).

where the density of losses is maximum. A better *a posteriori* evaluation might be obtained using the first magnetization instead of the anhysteretic behavior.

REFERENCES

[1] A. Daikoku *et al.*, "A high precision motor design method by finite element analysis considering stress distribution in stator core," in *Proc. IEEE Int. Conf. Electr. Mach. Drives*, May 2005, pp. 366–372.

[2] K. Fonteyn, A. Belahcen, and A. Arkkio, "Properties of electrical steel sheets under strong mechanical stress," *Pollack Periodica*, vol. 1, no. 1, pp. 93–104, 2006.

[3] D. Miyagi, N. Maeda, Y. Ozeki, K. Miki, and N. Takahashi, "Estimation of iron loss in motor core with shrink fitting using FEM analysis," *IEEE Trans. Magn.*, vol. 45, no. 3, pp. 1704–1707, Mar. 2009.

[4] K. Yamazaki and Y. Kato, "Iron loss analysis of interior permanent magnet synchronous motors by considering mechanical stress and deformation of stators and rotors," *IEEE Trans. Magn.*, vol. 50, no. 2, pp. 909–912, Feb. 2014, Art. ID 7022504.

[5] L. Daniel and O. Hubert, "An equivalent stress for the influence of multiaxial stress on the magnetic behavior," *J. Appl. Phys.*, vol. 105, no. 7, 07A313, 2009.

[6] S. Zeze, Y. Kai, T. Todaka, and M. Enokizono, "Vector magnetic characteristic analysis of a PM motor considering residual stress distribution with complex-approximated material modeling," *IEEE Trans. Magn.*, vol. 48, no. 11, pp. 3352–3355, Nov. 2012.

[7] A. A. Abdallh and L. Dupré, "The influence of magnetic material degradation on the optimal design parameters of electromagnetic devices," *IEEE Trans. Magn.*, vol. 50, no. 4, pp. 1–10, Apr. 2014.

[8] Y. Xu, Y. Wei, J. Zou, J. Li, W. Qi, and Y. Li, "Estimation of the iron loss in deep-sea permanent magnet motors considering seawater compressive stress," *Sci. World J.*, vol. 2014, 265816, Aug. 2014.

[9] A. Bergqvist and G. Engdahl, "A stress-dependent magnetic Preisach hysteresis model," *IEEE Trans. Magn.*, vol. 27, no. 6, pp. 4796–4798, Nov. 1991.

[10] A. Sipeky and A. Ivanyi, "Preisach-type stress-dependent magnetic vector hysteresis model," *Phys. B, Condens. Matter*, vol. 403, nos. 2–3, pp. 491–495, 2008.

[11] O. Bottauscio, A. Lovisolo, P. E. Roccato, M. Zucca, C. Sasso, and R. Bonin, "Modeling and experimental analysis of magnetostrictive devices: From the material characterization to their dynamic behavior," *IEEE Trans. Magn.*, vol. 44, no. 11, pp. 3009–3012, Nov. 2008.

[12] M. J. Sablik, H. Kwun, G. L. Burkhardt, and D. C. Jiles, "Model for the effect of tensile and compressive stress on ferromagnetic hysteresis," *J. Appl. Phys.*, vol. 61, no. 8, pp. 3799–3801, 1987.

[13] H. W. L. Naus, "Theoretical developments in magnetomechanics," *IEEE Trans. Magn.*, vol. 47, no. 9, pp. 2155–2162, Sep. 2011.

[14] C. P. Sasso, V. Basso, M. LoBue, and G. Bertotti, "Vector model for the study of hysteresis under stress," *J. Appl. Phys.*, vol. 87, no. 9, pp. 4774–4776, 2000.

[15] R. C. Smith and M. J. Dapino, "A homogenized energy framework for ferromagnetic hysteresis," *IEEE Trans. Magn.*, vol. 42, no. 7, pp. 1747–1769, Jul. 2006.

[16] V. François-Lavet, F. Henrotte, L. Stainier, L. Noels, and C. Geuzaine, "An energy-based variational model of ferromagnetic hysteresis for finite element computations," *J. Comput. Appl. Math.*, vol. 246, pp. 243–250, Jul. 2013.

[17] D. P. Bulte, "The pursuit of hysteresis in polycrystalline ferromagnetic materials under stress," *IEEE Trans. Magn.*, vol. 45, no. 1, pp. 83–87, Jan. 2009.

[18] M. J. Sablik and D. C. Jiles, "Coupled magnetoelastic theory of magnetic and magnetostrictive hysteresis," *IEEE Trans. Magn.*, vol. 29, no. 4, pp. 2113–2123, Jul. 1993.

[19] M. J. Sablik and D. C. Jiles, "Modeling the effects of torsional stress on hysteretic magnetization," *IEEE Trans. Magn.*, vol. 35, no. 1, pp. 498–504, Jan. 1999.

[20] M. J. Dapino, R. C. Smith, L. E. Faidley, and A. B. Flatau, "A coupled structural-magnetic strain and stress model for magnetostrictive transducers," *J. Intell. Mater. Syst. Struct.*, vol. 11, no. 2, pp. 135–152, Feb. 2000.

[21] O. Perevertov and R. Schäfer, "Influence of applied compressive stress on the hysteresis curves and magnetic domain structure of grain-oriented transverse Fe–3%Si steel," *J. Phys. D, Appl. Phys.*, vol. 45, no. 13, 135001, 2012.

[22] L. Daniel and N. Galopin, "A constitutive law for magnetostrictive materials and its application to Terfenol-D single and polycrystals," *Eur. Phys. J. Appl. Phys.*, vol. 42, no. 2, pp. 153–159, 2008.

[23] A. J. Bergqvist, "A simple vector generalization of the Jiles–Atherton model of hysteresis," *IEEE Trans. Magn.*, vol. 32, no. 5, pp. 4213–4215, Sep. 1996.

[24] L. Bernard, X. Mininger, L. Daniel, G. Krebs, F. Bouillault, and M. Gabsi, "Effect of stress on switched reluctance motors: A magneto-elastic finite-element approach based on multiscale constitutive laws," *IEEE Trans. Magn.*, vol. 47, no. 9, pp. 2171–2178, Sep. 2011.

[25] L. Daniel, "An analytical model for the effect of multiaxial stress on the magnetic susceptibility of ferromagnetic materials," *IEEE Trans. Magn.*, vol. 49, no. 5, pp. 2037–2040, May 2013.

[26] N. Buiron, L. Hirsinger, and R. Billardon, "A multiscale model for magneto-elastic couplings," *J. Phys. IV France*, vol. 9, p. 187, Sep. 1999.

[27] W. D. Armstrong, "Magnetization and magnetostriction processes in Tb(0.27-0.30)Dy(0.73-0.70)Fe(1.9-2.0)," *J. Appl. Phys.*, vol. 81, no. 5, pp. 2321–2326, Mar. 1997.

[28] D. C. Jiles and D. L. Atherton, "Theory of ferromagnetic hysteresis (invited)," *J. Appl. Phys.*, vol. 55, no. 6, pp. 2115–2120, 1984.

[29] A. Pulnikov et al., "The relation between the magnetostriction and the hysteresis losses in the non-oriented electrical steels," *J. Magn. Magn. Mater.*, vols. 290–291, pp. 1454–1456, Apr. 2005.

[30] J. V. Leite, N. Sadowski, P. Kuo-Peng, N. J. Batistela, J. P. A. Bastos, and A. A. de Espíndola, "Inverse Jiles–Atherton vector hysteresis model," *IEEE Trans. Magn.*, vol. 40, no. 4, pp. 1769–1775, Jul. 2004.

[31] J. V. Leite et al., "Real coded genetic algorithm for Jiles–Atherton model parameters identification," *IEEE Trans. Magn.*, vol. 40, no. 2, pp. 888–891, Mar. 2004.

[32] K. Chwastek and J. Szczyglowski, "Identification of a hysteresis model parameters with genetic algorithms," *Math. Comput. Simul.*, vol. 71, no. 3, pp. 206–211, May 2006.

[33] K. Chwastek, J. Szczyglowski, and M. Najgebauer, "A direct search algorithm for estimation of Jiles–Atherton hysteresis model parameters," *Mater. Sci. Eng. B*, vol. 131, nos. 1–3, pp. 22–26, Jul. 2006.

[34] K. Chwastek, "Modelling of dynamic hysteresis loops using the Jiles–Atherton approach," *Math. Comput. Model. Dyn. Syst.*, vol. 15, no. 1, pp. 95–105, 2009.

[35] R. Marion, R. Scorretti, N. Siauve, M. Raulet, and L. Krahenbuhl, "Identification of Jiles–Atherton model parameters using particle swarm optimization," *IEEE Trans. Magn.*, vol. 44, no. 6, pp. 894–897, Jun. 2008.

[36] M. LoBue, C. Sasso, V. Basso, F. Fiorillo, and G. Bertotti, "Power losses and magnetization process in Fe–Si non-oriented steels under tensile and compressive stress," *J. Magn. Magn. Mater.*, vols. 215–216, pp. 124–126, Jun. 2000.

[37] K. J. Stevens, "Stress dependence of ferromagnetic hysteresis loops for two grades of steel," *NDT&E Int.*, vol. 33, no. 2, pp. 111–121, Mar. 2000.

[38] Y. Kai, Y. Tsuchida, T. Todaka, and M. Enokizono, "Influence of stress on vector magnetic property under alternating magnetic flux conditions," *IEEE Trans. Magn.*, vol. 47, no. 10, pp. 4344–4347, Oct. 2011.

[39] M. Rekik, O. Hubert, and L. Daniel, "Influence of a multiaxial stress on the reversible and irreversible magnetic behaviour of a 3%Si–Fe alloy," *Int. J. Appl. Electromagn. Mech.*, vol. 44, nos. 3–4, pp. 301–315, 2014.

[40] D. C. Jiles, J. B. Thoelke, and M. K. Devine, "Numerical determination of hysteresis parameters for the modeling of magnetic properties using the theory of ferromagnetic hysteresis," *IEEE Trans. Magn.*, vol. 28, no. 1, pp. 27–35, Jan. 1992.

[41] D. Lederer, A. Kost, H. Igarashi, and T. Honma, "On the parameter identification and application of the Jiles–Atherton hysteresis model for numerical modelling of measured characteristics," *IEEE Trans. Magn.*, vol. 35, no. 3, pp. 1211–1214, May 1999.

[42] J. V. Leite, N. Sadowski, P. Kuo-Peng, N. J. Batistela, and J. P. A. Bastos, "The inverse Jiles–Atherton model parameters identification," *IEEE Trans. Magn.*, vol. 39, no. 3, pp. 1397–1400, May 2003.

[43] S. Cao, B. Wang, R. Yan, W. Huang, and Q. Yang, "Optimization of hysteresis parameters for the Jiles–Atherton model using a genetic algorithm," *IEEE Trans. Appl. Supercond.*, vol. 14, no. 2, pp. 1157–1160, Jun. 2004.

[44] J. Gyselinck, P. Dular, N. Sadowski, J. Leite, and J. P. A. Bastos, "Incorporation of a Jiles–Atherton vector hysteresis model in 2D FE magnetic field computations: Application of the Newton–Raphson method," *COMPEL, Int. J. Comput. Math. Elect. Electron. Eng.*, vol. 23, no. 3, pp. 685–693, 2004.

[45] F. I. Hantila, G. Preda, and M. Vasiliu, "Polarization method for static fields," *IEEE Trans. Magn.*, vol. 36, no. 4, pp. 672–675, Jul. 2000.

[46] E. Dlala, A. Belahcen, and A. Arkkio, "Locally convergent fixed-point method for solving time-stepping nonlinear field problems," *IEEE Trans. Magn.*, vol. 43, no. 11, pp. 3969–3975, Nov. 2007.

[47] F. Hecht, "New development in FreeFem++," *J. Numer. Math.*, vol. 20, nos. 3–4, pp. 251–266, 2012.

[48] X. Rain, M. Hilairet, and O. Bethoux, "Comparative study of various current controllers for the switched reluctance machine," in *Proc. IEEE Vehicle Power Propuls. Conf. (VPPC)*, Sep. 2010, pp. 1–6.

[49] S. E. Zirka, Y. I. Moroz, R. G. Harrison, and K. Chwastek, "On physical aspects of the Jiles–Atherton hysteresis models," *J. Appl. Phys.*, vol. 112, no. 4, 043916, 2012.

[50] L. Daniel, M. Rekik, and O. Hubert, "A multiscale model for magneto-elastic behaviour including hysteresis effects," *Arch. Appl. Mech.*, vol. 84, nos. 9–11, pp. 1307–1323, Oct. 2014.

[51] H. V. Sande, H. De Gersem, F. Henrotte, and K. Hameyer, "Solving nonlinear magnetic problems using Newton trust region methods," *IEEE Trans. Magn.*, vol. 39, no. 3, pp. 1709–1712, May 2003.

[52] J. C. Simo and R. L. Taylor, "A return mapping algorithm for plane stress elastoplasticity," *Int. J. Numer. Methods Eng.*, vol. 22, no. 3, pp. 649–670, Mar. 1986.

[53] I. R. Ciric and F. I. Hantila, "An efficient harmonic method for solving nonlinear time-periodic eddy-current problems," *IEEE Trans. Magn.*, vol. 43, no. 4, pp. 1185–1188, Apr. 2007.

[54] S. Ausserhofer, O. Biro, and K. Preis, "An efficient harmonic balance method for nonlinear eddy-current problems," *IEEE Trans. Magn.*, vol. 43, no. 4, pp. 1229–1232, Apr. 2007.

[55] M. d'Aquino, G. Rubinacci, A. Tamburrino, and S. Ventre, "Three-dimensional computation of magnetic fields in hysteretic media with time-periodic sources," *IEEE Trans. Magn.*, vol. 50, no. 2, pp. 53–56, 7001104, Feb. 2014.